Biomaterials 246 (2020) 119971

Contents lists available at ScienceDirect

Biomaterials

journal homepage: www.elsevier.com/locate/biomaterials

# Tumor microenvironment (TME)-activatable circular aptamer-PEG as an effective hierarchical-targeting molecular medicine for photodynamic therapy

Yu Yang[a,b], Wenjun Zhu[d], Liang Cheng[d], Ren Cai[b], Xuan Yi[d], Jiaxuan He[c], Xiaoshu Pan[b], Lu Yang[b], Kai Yang[d], Zhuang Liu[d], Weihong Tan[b,c,**], Meiwan Chen[a,*]

[a] State Key Laboratory of Quality Research in Chinese Medicine, Institute of Chinese Medical Sciences, University of Macau, Taipa, Macau
[b] Center for Research at Bio/Nano Interface, Department of Chemistry, Department of Physiology and Functional Genomics, Health Cancer Center, UF Genetics Institute, McKnight Brain Institute, University of Florida, Gainesville, FL, 32611-7200, USA
[c] Molecular Science and Biomedicine Laboratory, State Key Laboratory of Chemo/Biosensing and Chemometrics, College of Chemistry and Chemical Engineering, College of Life Sciences, Collaborative Innovation Center for Chemistry and Molecular Medicine, Hunan University, Changsha, 410082, China
[d] Institute of Functional Nano & Soft Materials Laboratory (FUNSOM), Soochow University, Suzhou, Jiangsu, 215123, China

ARTICLE INFO

*Keywords:*
Tumor microenvironment (TME)
Aptamer-drug conjugates (ApDCs)
Photodynamic therapy (PDT)
Deep tumor penetration

ABSTRACT

Photodynamic therapy (PDT) is an effective and noninvasive therapeutic strategy employing light-triggered singlet oxygen (SO) and reactive oxygen species (ROS) to kill lesional cells. However, for effective *in vivo* delivery of PDT agent into the cancer cells, various biological obstacles including blood circulation and condense extracellular matrix (ECM) in the tumor microenvironment (TME) need to be overcome. Furthermore, the enormous challenge in design of smart drug delivery systems is meeting the difference, even contradictory required functions, in different steps of the complicated delivery process. To this end, we present that TME-activatable circular pyrochlorophyll A (PA)-aptamer-PEG (PA-Apt–CHO–PEG) nanostructures, which combine the advantages of PEG and aptamer, would be able to realize efficient *in vivo* imaging and PDT. Upon intravenous (i.v.) injection, PA-Apt–CHO–PEG shows "stealth-like" long circulation in blood compartments without specific recognition capacity, but once inside solid tumor, PA-Apt–CHO–PEG nanostructures are cleaved and then form PA-Apt Aptamer-drug conjugations (ApDCs) *in situ*, allowing deep penetration into the solid tumor and specific recognition of cancer cells, both merits, considering anticipated future clinical translation of ApDCs.

## 1. Introduction

As an effective and noninvasive therapeutic strategy for diseases, primarily cancers, photodynamic therapy (PDT) employs photosensitizers (PS) under light irradiation to produce singlet oxygen (SO) and reactive oxygen species (ROS), to cause DNA damage and cell apoptosis [1–3]. However, because the generation of SO exhibits extremely short lifespans (< 200 ns) and short diffusion range (~20 nm) [4–6], it is essential to develop an approach for selective generation of SO in lesional areas for more efficient and reliable PDT with fewer side effects [7–11]. Aptamers [12–20], also called "chemical antibodies", with their flexible design, convenient modification, excellent chemical stability, high specificity and affinity and limited immunogenicity are important recognition elements of tumor. Aptamer could be easily conjugated with drugs or other molecules without loss of their activities. Recent studies showed that conjugating an aptamer to drug including PS (ApDCs) could efficiently enhance specific accumulation of active drug in the tumor tissue [21–25]. For instance, porphyrin derivatives, such as 5,10,15,20-Tetrakis-(*N*-methyl-4-pyridyl) porphine (TMPyP4), as photosensitizers could be loaded into G-quadruplex DNA sequences for efficient and selective *in vitro* destruction of cancer cells [13]. However, the *in vivo* application and clinical translation of ApDCs for targeted cancer treatment, including PDT, is limited by their low stability in the physiological environment and short blood circulation time [26–28].

For targeted delivery of active drug into the cytoplasm of cancer cells in solid tumors, various biological obstacles, including blood circulation and complicated tumor microenvironment (TME) must be

* Corresponding author.
** Corresponding author. Center for Research at Bio/Nano Interface, Department of Chemistry, Department of Physiology and Functional Genomics, Health Cancer Center, UF Genetics Institute, McKnight Brain Institute, University of Florida, Gainesville, FL, 32611-7200, USA.
*E-mail address:* mwchen@um.edu.mo (M. Chen).

https://doi.org/10.1016/j.biomaterials.2020.119971
Received 25 November 2019; Received in revised form 27 February 2020; Accepted 13 March 2020
Available online 14 March 2020
0142-9612/ 

overcome [29,30]. For a solid tumor, in addition to tumor cells, TME includes many other types of cells such as immune cells, bone marrow-derived inflammatory cells, lymphocytes and others, which are surrounded by tumor-associated fibroblasts and extracellular matrix (ECM), generating monstrous biological barriers for efficient delivery of anti-cancer agents [31–34]. Thus, prolonged blood circulation time without nonspecific adsorption during the blood circulation, and penetration deep into tumor tissues and specific recognition of tumor cells are favorable for improvement of delivery efficacy to target cancer cells [35–38]. However, during the tortuous delivery process, smart drug delivery systems must meet various, even contradictory, requirements in blood circulation and TME [39–41]. For instance, introduction of targeting ligands endows delivery systems with high selectivity and enhanced tumor accumulation, while, at the same time, shortening their blood circulation [29,42,43]. Additionally, for recognition of cancer cells in solid tumor, targeted delivery systems need to first deeply penetrate across the condensed extracellular collagen and matrix in the TME [44]. Interestingly, PEGylation can endow a "stealth" delivery system with prolonged blood circulation, but such strategy hinders the system's capacity for cellular internalization and then traps it inside the tumor, inducing gradual clearance by blood circulation and, hence, reducing the long-term effect [45–47]. Recently, many multistage and responsive nanocarriers have been designed to circumvent the delivery obstacles with different strategies, including negative-to-positive charge conversion, large-to-small size change, and PEGylation-dePEGylation [48,49]. Although several encouraging strategies have been reported in the design of smart responsive nanocarriers, they only focus on achieving relative mono-functionality and require elaborate and complicated synthesis and fabrication. This calls for the development of a simple and effective drug delivery system at the molecular level with prolonged blood circulation, deep tumor penetration, and highly selective and specific recognition of tumor cells for efficient *in vivo* cancer treatment.

Polyethylene glycol (PEG), a U.S. Food and Drug Administration (FDA)-approved compound, has been widely used as a modification agent to endow anticancer agents with "stealth-like" long blood circulation behavior, enhancing their tumor accumulation [50,51]. ApDCs have been developed as promising targeted drug delivery systems for enhanced cancer treatment efficacy with few side effects [22]. However, the biomedical applications of coupling the aptamer-PEG structure have been relatively less explored to date. Herein, we have designed a circular aptamer-PEG structure which is capable of prolonged blood circulation, and then responds to the acidic tumor microenvironment to deeply penetrate the solid tumor and selectively recognize cancer cells for *in vivo* targeted bioimaging and PDT. In a typical design, AS1411 aptamer containing G-rich oligonucleotide sequences with specific recognition of nucleolin, which is a non-ribosomal protein normally existing in the nucleus and also highly expressed on the surface of cancer cells [52], was chosen to be conjugated with pyrochlorophyll A (PA) [53], an efficient photosensitizer, to form PA-Apt ApDCs for *in vivo* targeted bioimaging and PDT The PA-Apt ApDCs with two terminal amino groups can be coupled by PEG with aldehyde groups on both termini via formation of Schiff base bonds to form PA-Apt–CHO–PEG. At physiological pH 7.4, PA-Apt–CHO–PEG with Schiff base bonds remains collodally stable to hinder cellular uptake by normal cells and prolong blood circulation. However, after entering TME at pH 6.5, the Schiff base bonds between aptamer and PEG would be rapidly cleaved to shed the PEG corona, inducing *in situ* formation of targeting ApDCs for penetration across the dense extracellular matrix and selective recognition of cancer cells. As evaluated by *in vitro* and *in vivo* experiments, our PA-Apt–CHO–PEG nanostructures were found to be efficient PDT agents with dramatic tumor inhibition efficacy. We first prepared TME-responsive PA-Apt–CHO–PEG nanostructures, which combine the advantages of both PEG, with long blood circulation and limited cellular uptake by normal cells, and ApDCs, with deep tumor tissue penetration and specific targeting of cancer cells, to design a facile and efficient drug delivery strategy, which is promising for future clinical translation of ApDCs.

## 2. Experimental section

### 2.1. Materials

Pyrochlorophyll A (PA) was purchased from Frontier Scientific, Inc. *N*-[ε-maleimidocaproic acid) hydrazide, trifluoroacetic acid salt (EMCH·TEA) and sulfosuccinimidyl-4-[*N*-maleimidomethyl]cyclohexane-1-carboxylate (Sulfo-SMCC crosslinker) were obtained from Thermo Fisher Scientific. Bifunctional poly(ethylene glycol), *N*-hydroxysuccinimide esters (NHS-PEG-NHS, MW = 6 K) and Hydroxylpoly (ethylene glycol) (MW = 6 K) were purchased from Biomatrik Inc. Dimethylformamide (DMF), 3-(4,5-dimethylthiazol-2-yl)-2,5-diphenyltetrazolium bromide (MTT), *N*-(3-dimethylaminopropyl)-*N*′-ethylcarbodiimide hydrochloride (EDC·HCl), 4-dimethylaminopyridine (DMAP), and dichloromethane (DCM) were purchased from Sigma-Aldrich.

**Synthesis of dialdehyde poly(ethylene glycol):** Dialdehyde poly (ethylene glycol) (CHO-PEG-CHO) was prepared following a previously reported protocol [30]. Briefly, 1 mmol of poly(ethylene glycol) was activated by adding 10 mmol of EDC·HCl and 0.4 mmol of DMAP in 30 mL of dichloromethane (DCM) solution. After adding 3 mmol of 4-carboxybenzaldehyde, the mixture was then reacted under magnetic stirring at room temperature for 48 h. After concentrating the solution by rotary evaporator, the mixture was washed 5 times with 5% NaCl, and then the organic layer was collected. After precipitating twice with excess diethylether and vacuum drying, the mixture was dialyzed against deionized water for 2 days to obtain the final product.

**Aptamers:** Aptamer AS1411, 5′-NH2-TTT(HS)TT TGG TGG TGG TGG TTG TGG TGG TGG TGG TT-NH2-3′, with disulfide group and two amino groups was synthesized using an ABI3400 DNA/RNA synthesizer (Applied Biosystems, Foster City, CA, USA). The final aptamer sequences were deprotected in APA solution (ammonium hydroxide/40% aqueous methylamine 1:1) at 65 °C for 30 min. After purification by reversed-phase HPLC (ProStar, Varian, Walnut Creek, CA, USA), the product was freeze-dried for further usage.

**Synthesis of Aptamer-PA conjugates:** Five μmol of pyrochlorophyll A (PA) and 5 mmol of *N*-[ε-maleimidocaproic acid) hydrazide and trifluoroacetic acid salt (EMCH·TEA) were dissolved in 1 mL of methanol and then stirred in the dark for 24 h at room temperature. TCEP was employed to reduce the –SH group of AS1411 aptamer (200 nmol) in PBS at pH 7.4 at room temperature for 2 h. Excess TCEP was removed using a Sephadex® G-25 column (Sigma-Aldrich). Next, the AS1411 aptamer solution was reacted with the prepared EMCH-PA dissolved in the DMF for 12 h. After purification by HPLC and subsequent freeze drying, the PA-Aptamer conjugates were obtained for further usage.

To prepare the pH-responsive PA-Apt–CHO–PEG nanostructure, 2 μmol of pre-prepared CHO-PEG-CHO were added to the above prepared Aptamer-PA conjugates (200 nmol) at pH 7.4 and then reacted another 24 h at room temperature in the dark. After ultra-centrifugation at 4000 rpm using 10 kDa Millipore filters to remove excess precursors, the purified PA-Apt–CHO–PEG nanostructure was collected for further usage. The nonresponsive PA-Apt–NHS–PEG nanostructure was obtained using the same approach, by replacing CHO-PEG-CHO with NH2-PEG-NH2.

### 2.2. Characterization

The hydrodynamic sizes of PA-Apt–CHO–PEG and PA-Apt–NHS–PEG incubated at different pH values were performed using dynamic light scattering (DLS) (Zetasizer Nano-ZS, Malvern Instruments, UK). UV–Vis–NIR absorption spectra of PA-Aptamer, PA-Apt–CHO–PEG and PA-Apt-NH2-PEG were measured using a

UV–Vis–NIR spectrometer (PerkinElmer Lambda 750).

### 2.3. Detection of singlet oxygen

PA-Apt–CHO–PEG and PA-Apt were exposed to 670-nm light for various time periods at power density of 5 mW/cm$^2$. Next, 2.5 μM of singlet oxygen sensor green dissolved in methanol (SOSG, Molecular Probes, USA) was added into different samples. Afterwards, the generated SO was determined by measuring the fluorescence intensity of SOSG at 530 nm under the condition excitation wavelength of 494 nm using SpectraMax® i3x Platform.

### 2.4. Cellular experiments

Nucleolin-overexpressing MCF-7 human breast cancer cells were cultured in DMEM medium containing 10% fetal bovine serum (FBS), 40U/ml insulin and 1% penicillin/streptomycin at 37 °C under 5% $CO_2$, conditions recommended by the American Type Culture Collection (ATCC).

Cell sample preparation for confocal and flow cytometry. MCF-7 cells were seeded in 12-well plates at a density of 5 × 10$^4$ cells per well and then incubated with PA-Apt, PA-Apt–NHS–PEG and PA-Apt–CHO–PEG in serum-free DMEM medium at pH 6.5 or pH 7.4. After culturing MCF-7 cells at 37 °C for 2 h, the cells were washed twice with cold PBS and then imaged by confocal imaging (LeciaSP5 laser scanning confocal microscope). The treated MCF-7 cells at 4 °C were also analyzed using a BD FACSCalibur™ platform.

To study *in vitro* PDT efficacy, MCF-7 cells were seeded in 96-well plates and incubated with various concentrations of free PA, PA-Apt, PA-Apt–NHS–PEG and PA-Apt–CHO–PEG at pH 6.5 or pH 7.4. After incubation for 2 h, the treated MCF-7 cells were washed twice with PBS and then irradiated by 670-nm light at the power density of 5 mW/cm$^2$ for 30 min. The cells were transferred to fresh DMEM cell culture medium for another 24 h incubation. Then, cell viability was measured using standard thiazolyltetrazolium (MTT, Sigma Aldrich) assay.

### 2.5. In vivo imaging

Balb/c mice were purchased from Sochoow University Laboratory Animal Center and used according to the approved protocol. To develop the tumor model, Balb/c mice pretreated with estrogens were injected with 50 μL serum-free DMEM medium containing 1 × 10$^7$ MCF-7 cells.

For *in vivo* fluorescence imaging, mice bearing nucleolin-overexpressing MCF-7 tumors were i.v.-injected with PA-Apt–NHS–PEG or PA-Apt–CHO–PEG (1 mg/kg, in terms of PA). *In vivo* fluorescence images at different time periods were attained with a Lumina III *in vivo* imaging system (PerkinElmer). 24 h after i.v. injection, the mice were sacrificed to collect their major organs, including the liver, spleen, kidneys, heart, lung and tumor for *ex vivo* imaging.

For labeling with $^{99m}$Tc, PA-Apt–NHS–PEG or PA-Apt–CHO–PEG nanostructure was mixed with 2 mCi of Technetium-99 m in the $^{99m}TcO_4^-$ form (obtained from Shanghai GMS Pharmaceutical Co., Ltd.) in the presence of 100 μL of $SnCl_2$. After 1-h reaction at room temperature, excess of $^{99m}$Tc was removed using ultrafiltration (molecular weight cutoff MWCO = 10 kDa). For SPECT imaging, MCF-7 tumor-bearing mice were i.v.-injected with $^{99m}$Tc-labeled PA-Apt–NHS–PEG or $^{99m}$Tc-labeled PA-Apt–CHO–PEG and then imaged using an *in vivo* animal SPECT (MILabs, Utrecht, the Netherlands) imaging system. In addition, at different time points after i.v. injection of $^{99m}$Tc-labeled PA-Apt–NHS–PEG or $^{99m}$Tc-labeled PA-Apt–CHO–PEG, 20 μL of blood sample were collected from each mouse for analysis of blood circulation. At the 24 h time point, tumor and major organs were collected to measure biodistribution.

### 2.6. In vivo PDT treatment

Mice bearing nucleolin-overexpressing MCF-7 human breast tumors were randomly divided into six groups (5 mice per group): Group 1, PBS; Group 2, PA-Apt–CHO–PEG; Group 3, PA with 670-nm light irradiation; Group 4, PA-Apt with 670-nm light irradiation; Group 5, PA-Apt–NHS–PEG with 670-nm light irradiation; Group 6, PA-Apt–CHO–PEG with 670-nm light irradiation. At 24 h post-i.v. injection of various PA derivatives (1 mg/kg, in terms of PA), *in vivo* PDT treatment was performed by 670-nm light irradiation at the power density of 12 mW/cm$^2$ for 1 h. Subsequent treatments were conducted 6 days after the first PDT therapy with the same processing parameters. Tumor sizes and body weights of the groups were measured and recorded every other day.

The tumor volume was calculated as tumor volume = (tumor length) × (tumor width)$^2$/2. Subsequently, relative tumor volumes were determined as V/V0 (V0 was the initial volume). At day 18, mice were sacrificed, tumor tissues and major organs were harvested, and paraffin sections were prepared for further TUNEL and H&E staining according to the manufacturers' protocols.

## 3. Results and discussion

AS1411, a well-known tumor-targeting aptamer, owing to its specific recognition of cell surface nucleolin and cellular internalization by endocytosis, was chosen as the model targeting aptamer [54]. In particular, amino groups were introduced on both the 3′ and 5′ ends of AS1411 aptamer, and a thiol modifier was inserted near the 5′-end (5′-NH2-TTT(HS)TT TGG TGG TGG TGG TTG TGG TGG TGG TGG TT-NH2-3′). The thiol modifier allowed covalent conjugation of AS1411 to pyrochlorophyll A (PA), a typical porphyrin derivative used as a photosensitizer, to form an AS1411-PA conjugate via *N*-(ε-Maleimidocaproic acid) hydrazide (EMCH), as bifunctional linker. After conjugation, the AS1411-PA conjugate was purified by HPLC (Supporting Fig. S1). Subsequently, the dual-amino-modified AS1411 aptamer was coupled with bifunctional PEG aldehyde (CHO-PEG-CHO) via formation of Schiff bases in neutral or alkaline condition to obtain responsive circular aptamer-PEG (PA-Apt–CHO–PEG) nanostructures. As a control, nonresponsive to pH circular aptamer-PEG (PA-Apt–NHS–PEG) nanostructures were formed based on an amidation reaction by using bifunctional PEG succinimidyl ester (NHS-PEG-NHS) to replace CHO-PEG-CHO. As observed in dynamic light scattering (DLS) measurements, both PA-Apt–CHO–PEG and PA-Apt–NHS–PEG nanostructures showed significantly enhanced hydrodynamic diameters (~50 nm), in comparison to Apt-PA ApDC at 7–8 nm, indicating the successful conjugation of Apt-PA and PEG. Interestingly, PA-Apt–CHO–PEG can be partly decomposed at the pH 6.9 (Fig. S2). Furthermore, after 30 min incubation at pH 6.5, the hydrodynamic size of PA-Apt–CHO–PEG was decreased to about 10 nm, indicating efficient decomposition of PA-Apt–CHO–PEG into Apt-PA (Fig. 1b). In contrast, nonresponsive PA-Apt–NHS–PEG remained stable at pH 6.5 with the hydrodynamic size of ~50 nm (Fig. 1c). As shown in Fig. 1d, gel electrophoresis was employed to further evaluate the formation of the circular aptamer-PEG nanostructure. The nonresponsive PA-Apt–NHS–PEG nanostructure always remained stable. However, while the generation of Schiff base bonds of responsive PA-Apt–CHO–PEG also promoted stability at pH 7.4, the nanostructure became labile and cleavable in an acidic environment of pH 6.5.

Next, the UV–vis–NIR absorption of various structures was measured by UV–vis–NIR spectroscopy (Fig. 1e). Similar to Apt-PA, both PA-Apt–CHO–PEG and PA-Apt–NHS–PEG exhibited the typical PA absorption band at 675 nm, suggesting efficient attachment of PA to these Apt-PEG nanostructures. Subsequently, the capacity of singlet oxygen (SO) generation among free PA, Apt-PA ApDCs, and circular Apt-PEG nanostructures, was detected using singlet oxygen sensor green (SOSG). As shown in Fig. S3, various types of PA derivatives (i.e. A-Apt and PA-

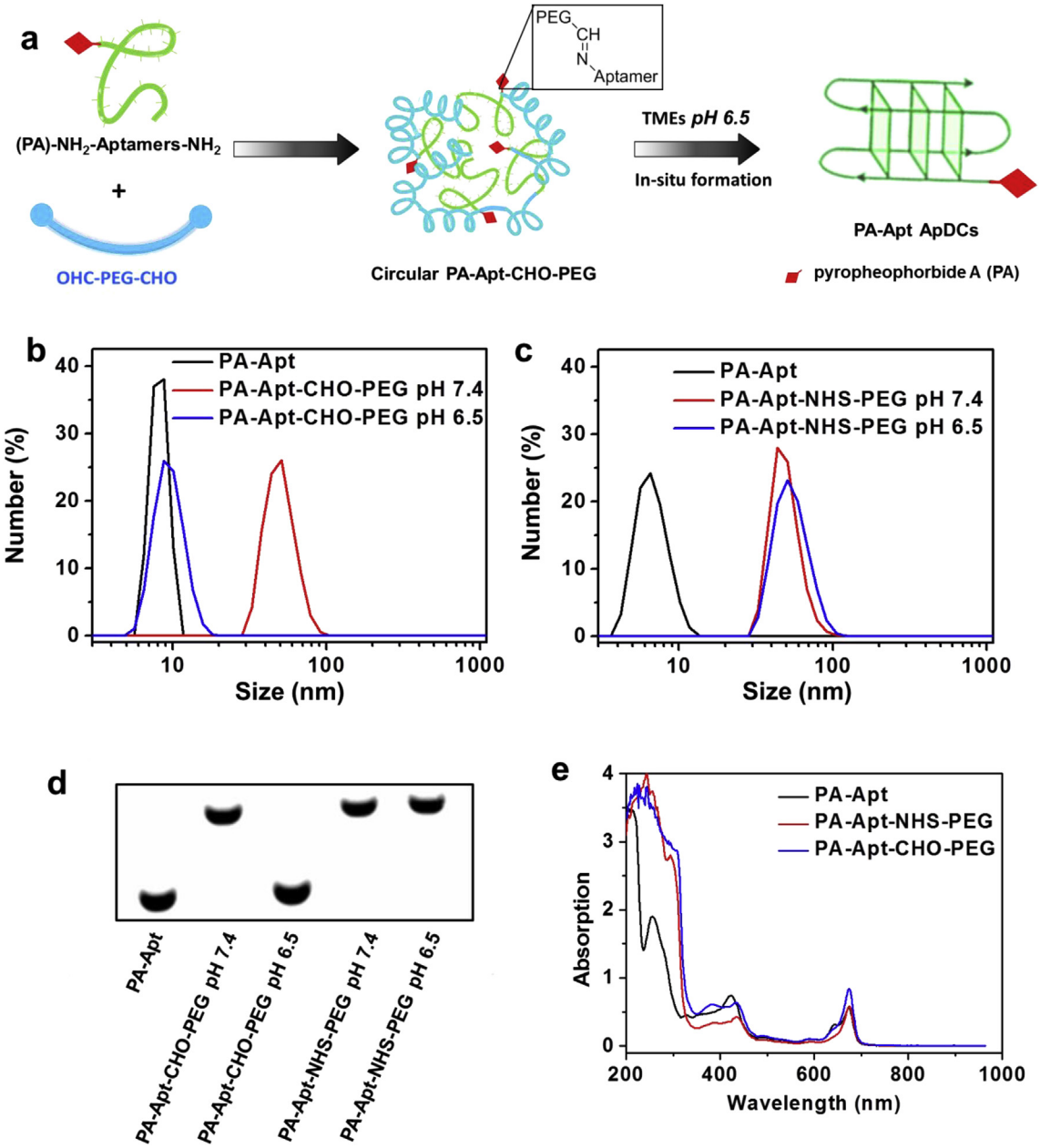


**Fig. 1.** Preparation and characterization of PA-Apt–CHO–PEG. (a) Schematic illustration for preparation of PA-Apt–CHO–PEG. (b–c) Hydrodynamic sizes of PA-Apt–CHO–PEG (b) and PA-Apt–NHS–PEG (c) incubated in PBS with different pH values for 30 min. (d) Gel electrophoresis analysis of PA-Apt–CHO–PEG and PA-Apt–NHS–PEG after treatment with different pH values. Compared to PA-Apt–NHS–PEG, pH-responsive PA-Apt–CHO–PEG nanostructures are labile and cleavable in an acidic environment at pH 6.5. (e) UV–vis–NIR spectra of PA-Apt, PA-Apt–CHO–PEG or PA-Apt–NHS–PEG.

Apt–CHO–PEG) exhibited no obvious difference in light-induced SO generation at the same PA concentration, allowing our structures to be used as efficient PS for PDT.

Next, we employed confocal imaging microscopy and flow cytometry to study pH-responsive cancer cell binding of the circular PA-Apt-PEG (PA-Apt–CHO–PEG and PA-Apt–NHS–PEG) nanostructure (Fig. 2a). Nucleolin-overexpressing MCF-7 human breast cancer cells were incubated with PA-Apt, PA-Apt–NHS–PEG, or PA-Apt–CHO–PEG for 2 h at 37 °C and washed with phosphate buffered saline (PBS) for removal of unbound nanostructure. As expected, strong fluorescence signals of PA were observed from the MCF-7 cells after treatment with PA-Apt, indicating strong binding affinity. However, after conjugation and capping with PEG to form the circular nanostructure, cell binding of PA-Apt–NHS–PEG and PA-Apt–CHO–PEG under neutral condition was significantly decreased. This was attributed to the conjugated PEG within the circular nanostructure, allowing efficient suppression of AS1411 G-quadruplex formation, which could specifically recognize and bind cell membrane surface nucleolin. Interestingly, strong fluorescence signals were observed for the PA-Apt–CHO–PEG-treated MCF-7 cells cultured in medium at pH 6.5 because the Schiff base bonds between Apt and PEG were cleaved in the slightly acidic pH 6.5, followed by the formation of ApDC for targeting delivery of PA. In contrast, the cells treated with PA-Apt–NHS–PEG at pH 6.5 showed weak fluorescence signals, because PA-Apt–NHS–PEG remained extremely stable without triggering formation of the AS1411 G-quadruplex at pH 6.5 (Fig. 2b). Quantitative flow cytometry data further confirmed that switching the cell culture pH from 7.4 to 6.5 allowed responsive PA-Apt–CHO–PEG to obviously recover nucleolin-specific binding affinity, while PA-Apt–NHS–PEG showed extremely weak binding affinity towards MCF-7 cells (Fig. 2c).

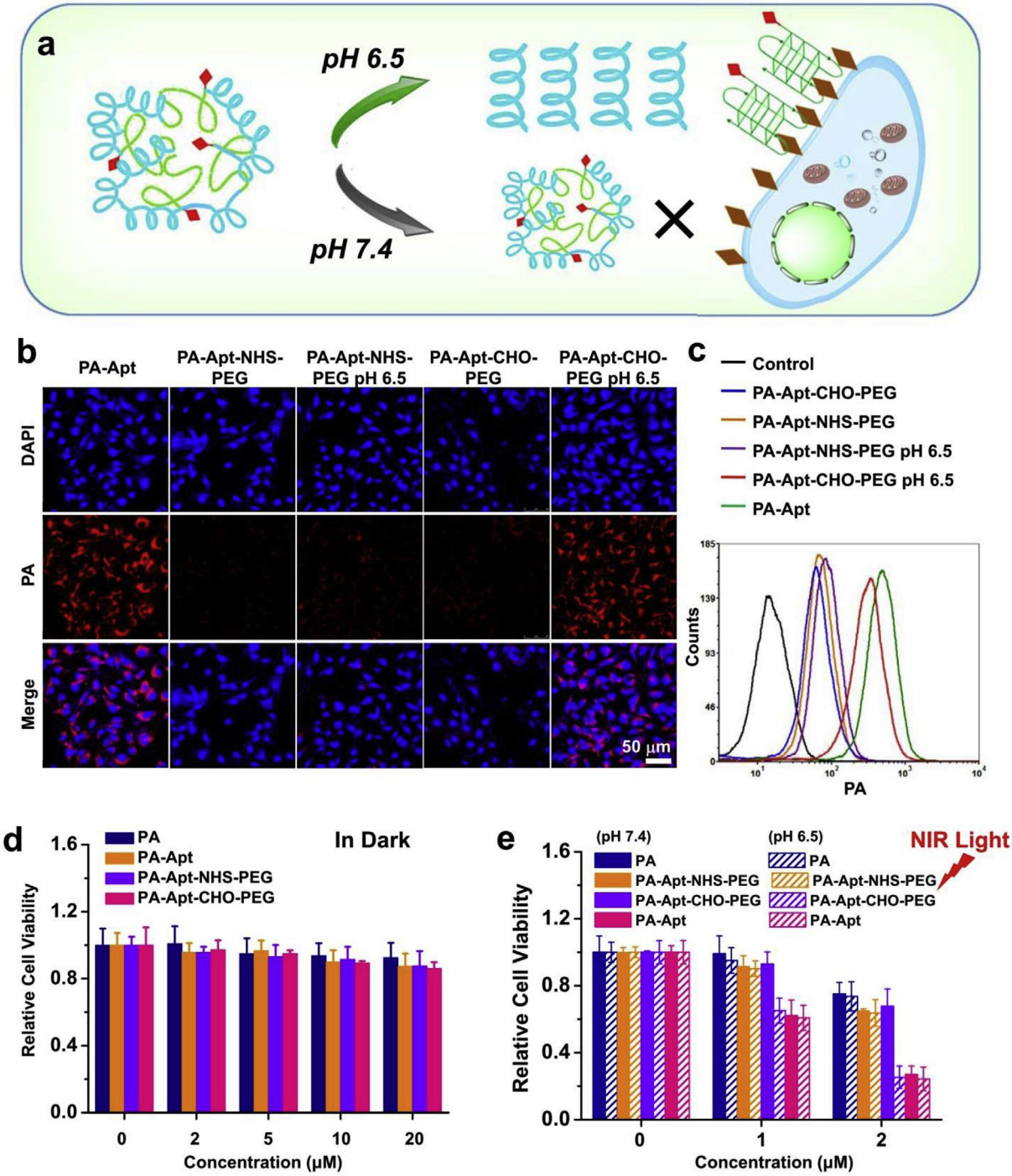


**Fig. 2.** pH-triggered specific recognition of cancer cells and *in vitro* PDT. (a) Schematic illustration for pH-activatable targeted cancer cell binding of PA-Apt–CHO–PEG. (b) Confocal images of MCF-7 cells incubated with PA-Apt, PA-Apt–NHS–PEG, and PA-Apt–CHO–PEG at pH 7.4 or 6.5 at 37 °C for 2 h. Scale bar: 50 μm. (c) Flow cytometry data of MCF-7 cells treated with PA-Apt, PA-Apt–NHS–PEG, and PA-Apt–CHO–PEG at pH 7.4 or 6.5 at 4 °C. (d) Relative cell viability of MCF-7 cells treated with various PA derivatives for 24 h in dark. (e) *In vitro* PDT treatments of MCF-7 cells after incubation with free PA, PA-Apt, PA-Apt–NHS–PEG, and PA-Apt–CHO–PEG at pH 7.4 or 6.5. PA-Apt–CHO–PEG showed enhanced *in vitro* PDT efficacy under reduced pH.

Encouraged by the obviously enhanced cellular binding affinity of PA-Apt–CHO–PEG at the reduced pH value, the *in vitro* PDT therapeutic effects of our responsive PA-Apt-PEG nanostructure were then investigated. As revealed by 3-[4,5-dimethylthiazole-2-yl]-2,5-diphenyltetrazolium bromide (MTT) cell viability assay, free PA, PA-Apt, PA-Apt–NHS–PEG, and PA-Apt–CHO–PEG in the dark did not show any obvious toxic effect to MCF-7 cells, demonstrating the excellent biocompatibility of these PA derivatives (Fig. 2d). Next, we measured intercellular $^1O_2$ generation after treatment of PA-Apt, PA-Apt–NHS–PEG, and PA-Apt–CHO–PEG at pH 7.4 or pH 6.5. As shown in Fig. S4, At pH 7.4, Only PA-Apt remaining specific targeting ability produced high PDT-induced intercellular $^1O_2$, while PA-Apt–NHS–PEG and PA-Apt–CHO–PEG lack of specific targeting ability generated moderate intercellular $^1O_2$. Interestingly, At pH 6.5, intercellular $^1O_2$ generation of PA-Apt–CHO–PEG-treated MCF-7 cells was obviously improved, because the Schiff base bonds between Apt and PEG were cleaved in the

slightly acidic pH 6.5, followed by the formation of ApDC for targeting delivery of PA. In contrast, the abilities of cells treated with PA-Apt or PA-Apt–NHS–PEG have no obvious changes in intracellular $^1O_2$ generation. To further evaluate the effect of pH on *in vitro* cancer killing efficiency of PA-Apt–CHO–PEG, PA-Apt conjugates were chosen as positive control, and nonresponsive PA-Apt–NHS–PEG based on amide bonds was employed as negative control. Next, MCF-7 cells incubated with free PA, PA-Apt, PA-Apt–NHS–PEG, and PA-Apt–CHO–PEG were cultured at either pH 7.4 or pH 6.5 for 2 h, washed with cold PBS, and then irradiated by 670-nm light for 30 min at a power density of 5 mW/cm$^2$. After another 24 h culture, compared with specific targeting of PA-Apt to achieve high targeting PDT efficiency, free PA, PA-Apt–NHS–PEG and PA-Apt–CHO–PEG demonstrated low cancer cell killing ability at pH 7.4. However, when the experiment was performed at pH 6.5, PA-Apt–CHO–PEG dramatically improved the phototoxicity towards MCF-7 cells, whereas the cancer killing efficiency of free PA and nonresponsive PA-Apt–NHS–PEG remained rather low, owing to the cleavage of the Schiff base bonds at pH 6.5 and *in situ* formation of AS1411 G-quadruplex for high binding affinity to MCF-7 cells (Fig. 2e). These results collectively showed that the PA-Apt–CHO–PEG nanostructure could be considered as an efficient pH-responsive PDT agent to enhance the efficacy of photodynamic therapy in the solid tumor with acidic tumor microenvironment (TME).

Again encouraged by the excellent *in vitro* PDT efficacy of PA-Apt–CHO–PEG response to the reduced pH value, we investigated the *in vivo* tumor-targeting behavior of our pH-responsive nanostructures. Balb/c mice bearing MCF-7 tumors were intravenously (i.v.) injected with PA-Apt–CHO–PEG or PA-Apt–NHS–PEG and then imaged by a Lumina III *in vivo* imaging system (PerkinElmer) at different time points (Fig. 3a). The fluorescence of PA was distributed throughout mouse body at the early time points, but strong PA fluorescence signals were observed in tumor at 24 h post-injection (p.i.) of PA-Apt–CHO–PEG. However, much weaker PA fluorescence was detected in the tumors of mice treated with PA-Apt–NHS–PEG, indicating the specific tumor binding capacity of PA-Apt–CHO–PEG in the acidic TME. This phenomenon could be attributed to the Schiff base bonds inside the PA-Apt–CHO–PEG nanostructure, which were cleaved in acidic TME, followed by *in situ*-triggered AS1411 to form a G-quadruplex, exposing AS1411 aptamer to recognize the cancer cells.

As a consequence of fluorescence quenching and low signal-to-noise ratio of PA under *in vivo* physiological conditions, *in vivo* fluorescence imaging could not exactly track the *in vivo* behavior of our nanostructures. The porphyrin structure of PA allows incorporation of $^{99m}$Tc (Fig. 3b), which emits γ-rays and shows the extensive application in clinical single-photon emission computed tomography (SPECT) [55]. Consequently, $^{99m}$Tc-chelated PA-Apt–CHO–PEG nanostructure was employed to observe the accurate biodistribution profiles of our nanostructures by SPECT imaging. After mixing with $^{99m}$Tc, but without additional chelator molecules, $^{99m}$Tc-chelated PA-Apt-PEG exhibited excellent radiolabeling stability at 37 °C (Fig. 3c). Next, mice bearing MCF-7 tumors after i.v. injection of $^{99m}$Tc-PA-Apt–CHO–PEG or $^{99m}$Tc-PA-Apt–NHS–PEG were imaged by *in vivo* SPECT imaging. Compared to the mice treated with $^{99m}$Tc-PA-Apt–NHS–PEG, which showed no obvious gamma signals, $^{99m}$Tc-PA-Apt–CHO–PEG demonstrated strong tumor accumulation in a time-dependent manner, consistent with the uncovered *in vivo* fluorescence imaging results (Fig. 3d). Quantitative data obtained from region-of-interest (ROI) analysis of the SPECT images further illustrated that the accumulation in tumor had greatly increased from 3.16 ± 0.23% to 6.42 ± 0.45% from 0.5 h to 24 h p.i., respectively (Fig. 3e).

In addition to *in vivo* SPECT imaging, the *in vivo* behavior of $^{99m}$Tc-PA-Apt–NHS–PEG or $^{99m}$Tc-PA-Apt–CHO–PEG was quantitatively investigated by measuring *ex vivo* radioactivities. It was found that the blood levels of $^{99m}$Tc-PA-Apt–NHS–PEG or $^{99m}$Tc-PA-Apt–CHO–PEG exhibited relatively long blood circulation half-lives ($t_{1/2\alpha}$ = 0.82 ± 0.18, $t_{1/2\beta}$ = 7.28 ± 1.92; $t_{1/2\alpha}$ = 0.71 ± 0.106 h, $t_{1/2\beta}$ = 6.79 ± 0.44 h, respectively) and that both remained at the relatively high level of ~5%, even at 24 h p.i. (Fig. 3f). Next, we studied the biodistribution of the circular nanostructures by *ex vivo* measurement of radioactivity in different organs (Fig. 3g). At 24 h p.i., both $^{99m}$Tc-PA-Apt–CHO–PEG and $^{99m}$Tc-PA-Apt–NHS–PEG exhibited comparable accumulation in the liver and spleen, owing to phagocytosis of foreign materials and particles by the reticuloendothelial systems. Notably, $^{99m}$Tc-PA-Apt–CHO–PEG showed high tumor uptake, which was calculated to be at 6.22 ± 0.55 percent-of-injected-dose-per-gram-tissue (%ID/g) in comparison to $^{99m}$Tc-PA-Apt–NHS–PEG with tumor accumulation at 2.75 ± 0.31 %ID/g. Therefore, these results collectively illustrate that our pH-responsive PA-Apt–CHO–PEG nanostructures have prolonged blood circulation and that TME-responsive specific binding tumor cells would be particularly suitable for highly efficient tumor-targeting delivery, especially in solid tumors with low TME pH.

Owing to the efficient decomposition and size reduction of PA-Apt–CHO–PEG in the weak acidic environment, we then studied its interstitial penetration behavior inside solid tumor (Fig. 4a). As a control, nonresponsive circular PA-Apt–NHS–PEG with similar sizes conjugated by amino bonds remained structurally stable without loss of size at the reduced pH values. Tumor slices collected from mice i.v.-injected with PA-Apt, PA-Apt–CHO–PEG or PA-Apt–$NH_2$–PEG were stained with anti-CD31 to visualize the blood vessels for confocal imaging. As shown in Fig. 4b and c, for mice injected with PA-Apt–NHS–PEG, PA signals were observed near and even partly colocalized with anti-CD31-stained blood vessels, indicating that nonresponsive PA-Apt–NHS–PEG with relatively large particle sizes showed moderate tumor accumulation, but only limited interstitial diffusion inside the tumor. Meanwhile, PA-Apt ApDCs with smaller sizes exhibited excellent tumor penetration capacity, yet relatively limited tumor retention, owing to its short blood circulation and weak stability in the physiological environment. Notably, a large amount of PA fluorescence signals (cyan) were observed far from the anti-CD31-stained blood vessels, suggesting efficient tumor accumulation and very deep penetration of the PA-Apt–CHO–PEG nanostructure in the solid tumor. These results could be attributed to the relatively large size and high stability of PA-Apt–CHO–PEG in the blood circulation, leading to efficient tumor accumulation and retention. Once inside the tumor tissues, TME-responsive decomposition occurs with the subsequent release of ApDCs which are much smaller and more capable of deep interstitial penetration and effective tumor-targeted therapy.

Next, the efficacy of PA-Apt–CHO–PEG nanostructures for enhanced PDT was investigated with the MCF-7 mouse tumor model. In our *in vivo* PDT experiments, mice bearing MCF-7 tumors were randomly divided into six groups: Group 1, PBS; Group 2, PA-Apt–CHO–PEG; Group 3, PA with 670-nm light irradiation (PA + L); Group 4, PA-Apt with 670-nm light irradiation (PA-Apt + L); Group 5, PA-Apt–NHS–PEG with 670-nm light irradiation (PA-Apt–NHS–PEG + L); Group 6, PA-Apt–CHO–PEG with 670-nm light irradiation (PA-Apt–CHO–PEG + L). At 24 h post-i.v. injection of the various PA derivatives (1 mg/kg, in terms of PA), PDT was performed by 670-nm light irradiation at the power density of 12 mW/cm$^2$ for 1 h. Subsequent treatments were conducted 6 days after the first PDT therapy with the same processing parameters. The tumor sizes were measured with a digital caliper every two days during the entire treatment period, and the tumors from various treatment groups were collected (Fig. 5a), photographed, and then weighed at day 18 post-treatment (Fig. 5b and c). It was found that PA-Apt–CHO–PEG without 670-nm light irradiation showed no tumor inhibition effect and that free PA plus 670-nm light had only marginal inhibitory effect on tumor growth, most likely because of rather low tumor accumulation of PA. Compared to treatment of PA + L, mice treated with PA-Apt + L or PA-Apt–NHS–PEG + L exhibited enhanced tumor inhibition, as a result of specific targeting delivery of PA to tumor cells or prolonged blood circulation of PA derivatives, respectively. Growth of tumors in mice treated with PA-Apt–CHO–PEG and 670-nm

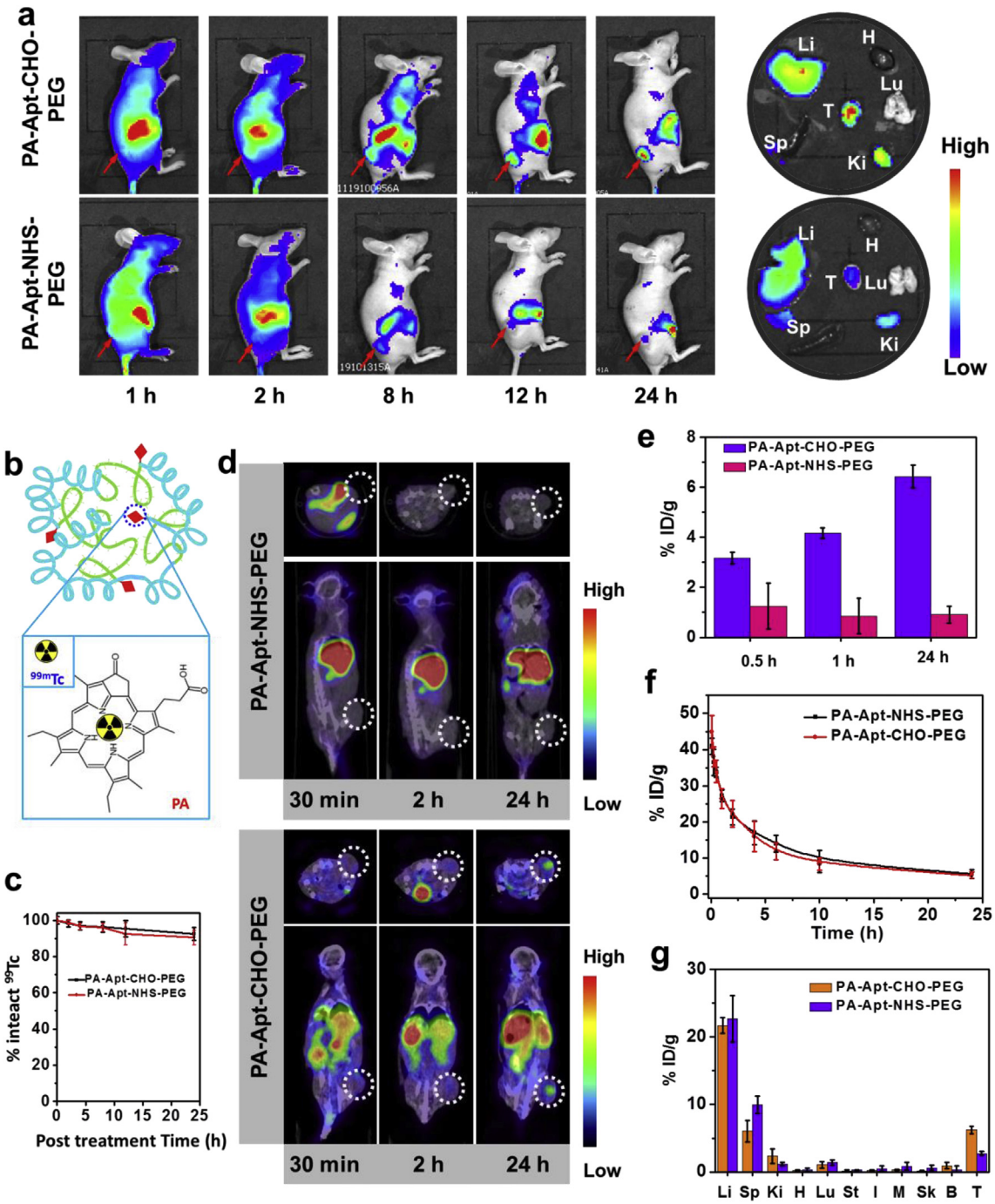


**Fig. 3.** *In vivo* imaging of mice bearing MCF-7 tumors post-i.v. injection of PA-Apt–NHS–PEG or PA-Apt–CHO–PEG. (a) *In vivo* fluorescence images of MCF-7 tumor-bearing mice after injection of PA-Apt–NHS–PEG or PA-Apt–CHO–PEG through tail vein. (b) Schematic illustration of $^{99m}$Tc-labeled PA inside the circular PA-Apt-PEG. (c) Radiolabeling stability of $^{99m}$Tc-labeled PA-Apt–NHS–PEG or $^{99m}$Tc-labeled PA-Apt–CHO–PEG in PBS at various time points. (d) *In vivo* SPECT imaging of MCF-7 tumor-bearing mice after i.v. injection of $^{99m}$Tc-PA-Apt–NHS–PEG or $^{99m}$Tc-PA-Apt–CHO–PEG. (e) Quantification of SPECT signals in tumor of mice taken at different time points after i.v. injection of $^{99m}$Tc-PA-Apt–NHS–PEG or $^{99m}$Tc-PA-Apt–CHO–PEG. (f–g) Blood circulation profiles (f) and biodistribution (24 h p.i.) profiles of $^{99m}$Tc-PA-Apt–NHS–PEG or $^{99m}$Tc-PA-Apt–CHO–PEG in mice post-i.v. injection. H, Li, Sp, Lu, Ki, St, I, M, Sk, B and T stand for heart, liver, spleen, lung, kidneys, stomach, intestine, muscle, skin, bone and tumor, respectively.

irradiation was sufficiently curbed, showing the highest antitumor efficacy of all treatments. Next, hematoxylin and eosin (H&E) staining and terminal deoxynucleotidyl transferase-mediated dUTP-biotin nick end labeling (TUNEL) staining of tumor slices was employed to further evaluate the enhanced PDT efficacy. The group treated with PA-Apt–CHO–PEG and 670-nm irradiation showed the most severe tumor cell damage with condensed nuclei, additional vacuoles and changed cell shapes revealed by H&E staining (Fig. 5d). Furthermore, Based on TUNEL staining, tumor on the mice treated with PA-Apt–CHO–PEG + L showed the highest apoptosis levels, following the same trend as H&E results. During treatment, mice in the treatment group (PA-Apt–CHO–PEG + L) showed normal behavior, and their body weight remained stable throughout the experiment (Supporting Fig. S5). To further study the physiological toxicity of PA-Apt–CHO–PEG, major organs, including liver, spleen, kidney, heart and lung, were harvested and sectioned for H&E staining after 18 days of treatment (Supporting Fig. S6), and no

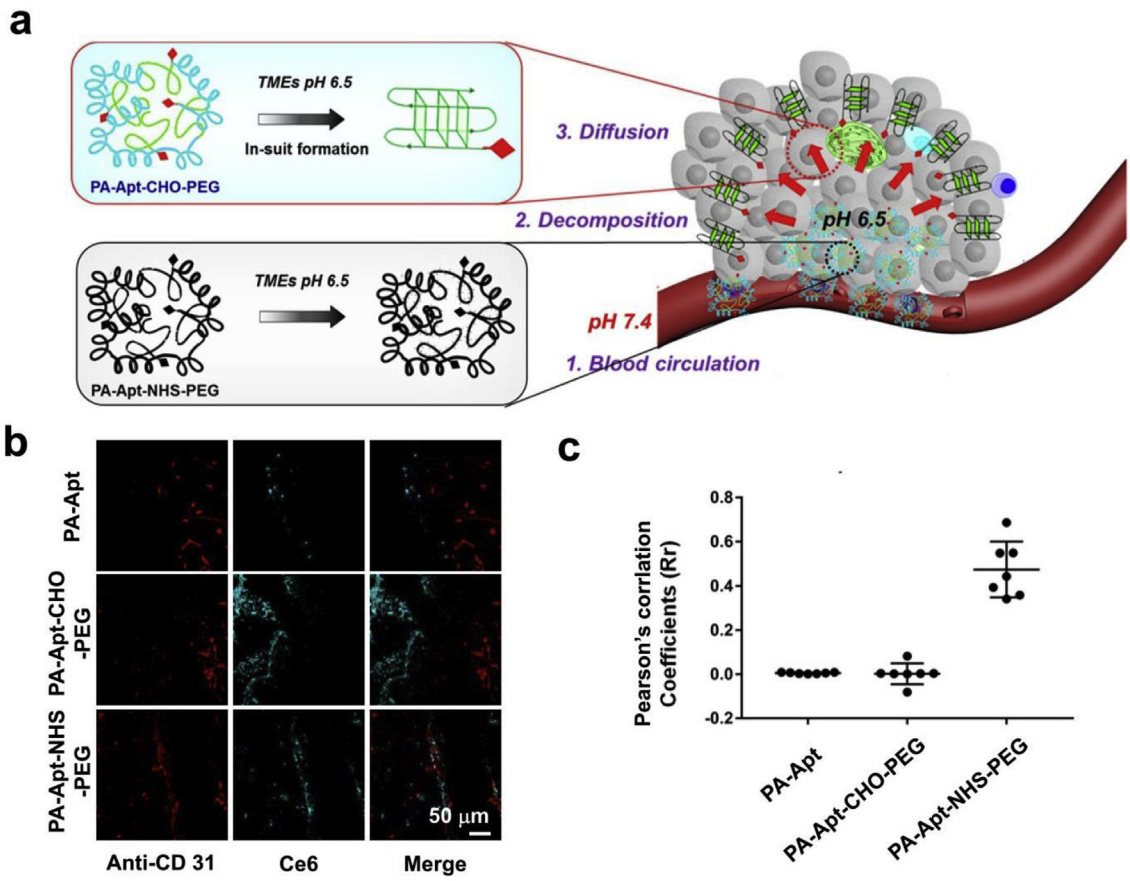


**Fig. 4.** *In vivo* PDT using PA-Apt–CHO–PEG. (a) Schematic illustration for TME-responsive decomposition of PA-Apt–CHO–PEG to release ApDCs for deep interstitial penetration and effective tumor-targeted therapy. (b) Confocal imaging collected from mice treated with PA-Apt, PA-Apt–NHS–PEG, or PA-Apt–CHO–PEG. The cyan and red signals stand for PA fluorescence and anti-CD31-stained blood vessels, respectively. (c) The quantification of Pearson's correlation coefficient (Rr) from (b). A higher value of Rr stands for a higher level of colocalization of fluorescent signals between PA and blood vessels. (For interpretation of the references to colour in this figure legend, the reader is referred to the Web version of this article.)

obvious signs of abnormality or acute toxicity of those PA-Apt–CHO–PEG nanostructures were evident in the treated mice.

## 4. Conclusion

In conclusion, we have designed and constructed a closely coupled PA-Apt–CHO–PEG nanostructure for *in vivo* TME-triggered targeted bioimaging and PDT. Compared to traditional ApDCs, the PA-Apt–CHO–PEG nanostructure demonstrated prolonged blood circulation and retention, owing to conjugated PEG, which endows the nanostructure with “stealth-like” behavior without specific recognition capability. Once inside solid tumor with acidic TME, however, the cleavage of Schiff base bonds between aptamer and PEG induced the decomposition of the conjugated PA-Apt–CHO–PEG structure, allowing *in situ* formation of ApDCs for diffusion deep inside the tumor, specifically targeting cancer cells. As a result of these mechanisms acting together, highly efficient *in vivo* PDT was achieved after systemic injection of PA-Apt–CHO–PEG into mice at rather low doses. Based on the excellent *in vivo* performance of the pH-responsive PA-Apt–CHO–PEG nanostructure, we have developed a facile, yet efficient, strategy for clinical application of ApDCs.

## CRediT authorship contribution statement

**Yu Yang:** Conceptualization, Methodology, Software, Writing - original draft, Data curation. **Wenjun Zhu:** Methodology, Software, Data curation. **Liang Cheng:** Data curation, Validation. **Ren Cai:** Validation. **Xuan Yi:** Investigation. **Jiaxuan He:** Methodology. **Xiaoshu Pan:** Software. **Lu Yang:** Investigation. **Kai Yang:** Data curation, Validation. **Zhuang Liu:** Writing - review & editing. **Weihong Tan:** Writing - review & editing. **Meiwan Chen:** Supervision, Funding acquisition, Writing - review & editing.

## Declaration of competing interest

The authors declare that they have no known competing financial interests or personal relationships that could have appeared to influence the work reported in this paper.

## Acknowledgements

The authors are grateful to Dr. Kathryn Williams for her critical comments during the preparation of this manuscript. This work is supported by grants awarded by the Macao Science and Technology Development Fund (083/2017/A2), the Research Fund of the University of Macau (MYRG2017-00182-ICMS), and the NSFC (NSFC 21221003 and NSFC 21327009).

## Appendix A. Supplementary data

Supplementary data to this article can be found online at https://doi.org/10.1016/j.biomaterials.2020.119971.

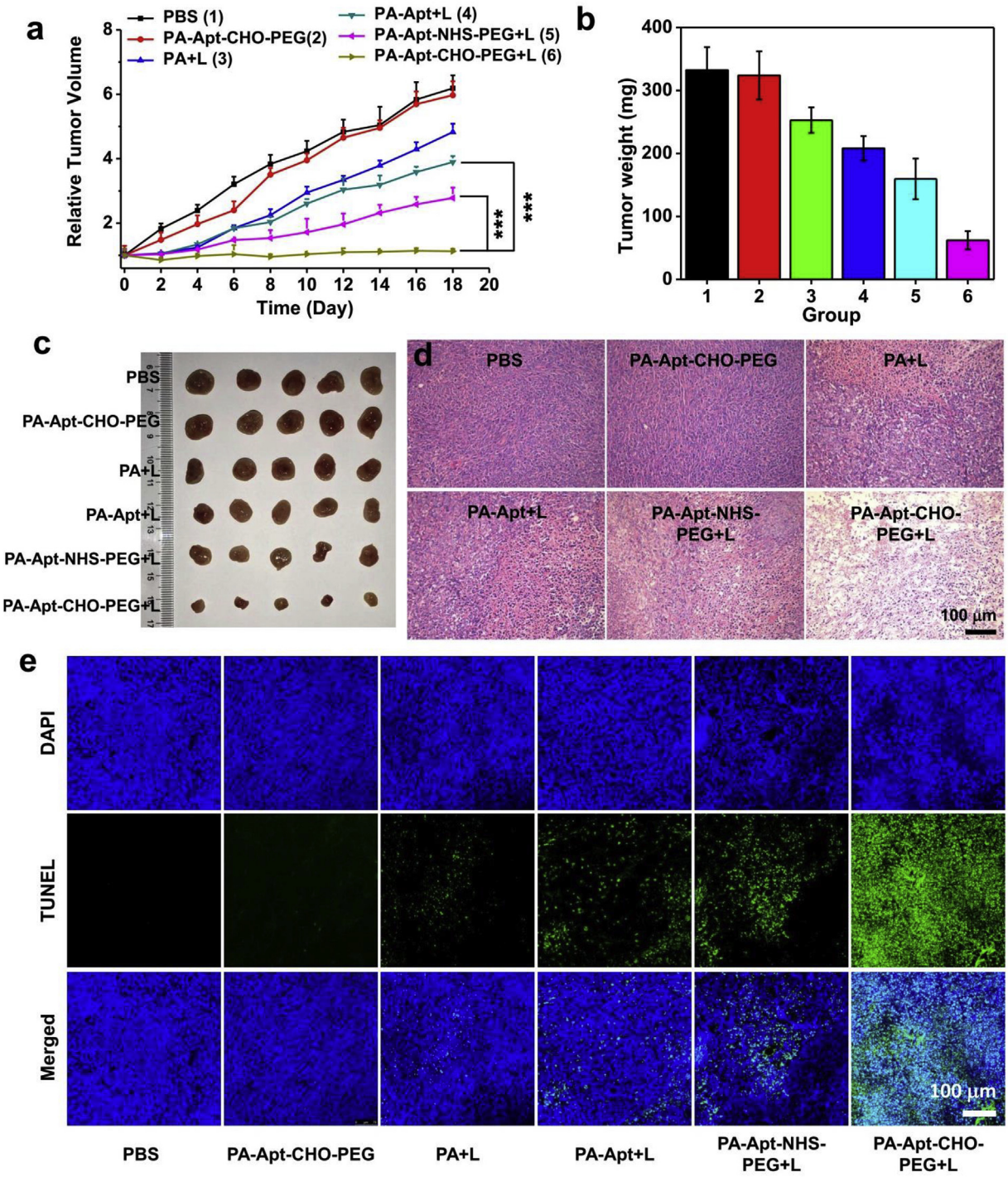


**Fig. 5.** (a) Tumor growth curves of MCF-7 tumor-bearing mice after various treatments, as indicated. *In vivo* PDT treatment was performed by 670-nm light irradiation at the density of 12 mW/cm$^2$ for 60 min. (b–c) Average weights (b) and photographs (c) of tumors from different groups collected at the 18th day after initiation of treatments. (d) H&E-stained tumor slices collected from different groups of mice at 2 days post-treatment. (e) Micrographs of TUNEL stained tumor slices collected from mice at 2 days post-treatment. Blue and green signals represent DAPI-stained cell nuclei and TUNEL-stained apoptotic cells, respectively. (For interpretation of the references to colour in this figure legend, the reader is referred to the Web version of this article.)

## References

[1] J. Liu, Y. Yang, W. Zhu, X. Yi, Z. Dong, X. Xu, M. Chen, K. Yang, G. Lu, L. Jiang, Nanoscale metal− organic frameworks for combined photodynamic & radiation therapy in cancer treatment, Biomaterials 97 (2016) 1–9.

[2] T.J. Dougherty, C.J. Gomer, B.W. Henderson, G. Jori, D. Kessel, M. Korbelik, J. Moan, Q. Peng, Photodynamic therapy, JNCI, J. Natl. Cancer Inst. 90 (12) (1998) 889–905.

[3] D.E. Dolmans, D. Fukumura, R.K. Jain, Photodynamic therapy for cancer, Nat. Rev. Canc. 3 (5) (2003) 380–387.

[4] L. Packer, K. Fuehr, Low oxygen concentration extends the lifespan of cultured human diploid cells, Nature 267 (5610) (1977) 423.

[5] R.G. Zepp, N.L. Wolfe, G. Baughman, R.C. Hollis, Singlet oxygen in natural waters, Nature 267 (5610) (1977) 421.

[6] K. Lu, C. He, W. Lin, Nanoscale metal–organic framework for highly effective photodynamic therapy of resistant head and neck cancer, J. Am. Chem. Soc. 136 (48) (2014) 16712–16715.

[7] Q. Yuan, Y. Wu, J. Wang, D. Lu, Z. Zhao, T. Liu, X. Zhang, W. Tan, Targeted bioimaging and photodynamic therapy nanoplatform using an aptamer-guided G-quadruplex DNA carrier and near-infrared light, Angew. Chem. Int. Ed. 52 (52) (2013) 13965–13969.

[8] W.M. Sharman, J.E. van Lier, C.M. Allen, Targeted photodynamic therapy via receptor mediated delivery systems, Adv. Drug Deliv. Rev. 56 (1) (2004) 53–76.
[9] N.M. Idris, M.K. Gnanasammandhan, J. Zhang, P.C. Ho, R. Mahendran, Y. Zhang, In vivo photodynamic therapy using upconversion nanoparticles as remote-controlled nanotransducers, Nat. Med. 18 (10) (2012) 1580.
[10] B.W. Henderson, T.J. Dougherty, How does photodynamic therapy work? Photochem. Photobiol. 55 (1) (1992) 145–157.
[11] X. Ji, Y. Kang, J. Ouyang, Y. Chen, D. Artzi, X. Zeng, Y. Xiao, C. Feng, B. Qi, N.Y. Kim, Synthesis of ultrathin biotite nanosheets as an intelligent theranostic platform for combination cancer therapy, Advanced Science 6 (19) (2019) 1901211.
[12] T. Hermann, D.J. Patel, Adaptive recognition by nucleic acid aptamers, Science 287 (5454) (2000) 820–825.
[13] Y.-A. Shieh, S.-J. Yang, M.-F. Wei, M.-J. Shieh, Aptamer-based tumor-targeted drug delivery for photodynamic therapy, ACS Nano 4 (3) (2010) 1433–1442.
[14] H.-M. Meng, H. Liu, H. Kuai, R. Peng, L. Mo, X.-B. Zhang, Aptamer-integrated DNA nanostructures for biosensing, bioimaging and cancer therapy, Chem. Soc. Rev. 45 (9) (2016) 2583–2602.
[15] D. Shangguan, Y. Li, Z. Tang, Z.C. Cao, H.W. Chen, P. Mallikaratchy, K. Sefah, C.J. Yang, W. Tan, Aptamers evolved from live cells as effective molecular probes for cancer study, Proc. Natl. Acad. Sci. Unit. States Am. 103 (32) (2006) 11838–11843.
[16] Y. Yang, J. Liu, X. Sun, L. Feng, W. Zhu, Z. Liu, M. Chen, Near-infrared light-activated cancer cell targeting and drug delivery with aptamer-modified nanostructures, Nano Res. 9 (1) (2016) 139–148.
[17] G. Zhu, J. Zheng, E. Song, M. Donovan, K. Zhang, C. Liu, W. Tan, Self-assembled, aptamer-tethered DNA nanotrains for targeted transport of molecular drugs in cancer theranostics, Proc. Natl. Acad. Sci. Unit. States Am. 110 (20) (2013) 7998–8003.
[18] K. Chen, B. Liu, B. Yu, W. Zhong, Y. Lu, J. Zhang, J. Liao, J. Liu, Y. Pu, L. Qiu, Advances in the development of aptamer drug conjugates for targeted drug delivery, Wiley Interdiscip. Rev.: Nanomed. Nanobiotechnol. 9 (3) (2017).
[19] H. Kuai, Z. Zhao, L. Mo, H. Liu, X. Hu, T. Fu, X. Zhang, W. Tan, Circular bivalent aptamers enable in vivo stability and recognition, J. Am. Chem. Soc. 139 (27) (2017) 9128–9131.
[20] Y. Wu, L. Zhang, C. Cui, S. Cansiz, H. Liang, C. Wu, I.-T. Teng, W. Chen, Y. Liu, W. Hou, Enhanced targeted gene transduction: AAV2 vectors conjugated to multiple aptamers via reducible disulfide linkages, J. Am. Chem. Soc. 140 (1) (2018) 2–5.
[21] Y.F. Huang, D. Shangguan, H. Liu, J.A. Phillips, X. Zhang, Y. Chen, W. Tan, Molecular assembly of an aptamer–drug conjugate for targeted drug delivery to tumor cells, Chembiochem 10 (5) (2009) 862–868.
[22] G. Zhu, G. Niu, X. Chen, Aptamer–drug conjugates, Bioconjugate Chem. 26 (11) (2015) 2186–2197.
[23] F. Li, J. Lu, J. Liu, C. Liang, M. Wang, L. Wang, D. Li, H. Yao, Q. Zhang, J. Wen, A water-soluble nucleolin aptamer-paclitaxel conjugate for tumor-specific targeting in ovarian cancer, Nat. Commun. 8 (1) (2017) 1390.
[24] Y. Yang, W. Zhu, Z. Dong, Y. Chao, L. Xu, M. Chen, Z. Liu, 1D coordination polymer nanofibers for low-temperature photothermal therapy, Adv. Mater. (2017).
[25] W. Tan, H. Wang, Y. Chen, X. Zhang, H. Zhu, C. Yang, R. Yang, C. Liu, Molecular aptamers for drug delivery, Trends Biotechnol. 29 (12) (2011) 634–640.
[26] C. Pestourie, B. Tavitian, F. Duconge, Aptamers against extracellular targets for in vivo applications, Biochimie 87 (9–10) (2005) 921–930.
[27] Y.-H. Lao, K.K. Phua, K.W. Leong, Aptamer nanomedicine for cancer therapeutics: barriers and potential for translation, ACS Nano 9 (3) (2015) 2235–2254.
[28] J.P. Dassie, P.H. Giangrande, Current progress on aptamer-targeted oligonucleotide therapeutics, Ther. Deliv. 4 (12) (2013) 1527–1546.
[29] Q. Sun, X. Sun, X. Ma, Z. Zhou, E. Jin, B. Zhang, Y. Shen, E.A. Van Kirk, W.J. Murdoch, J.R. Lott, Integration of nanoassembly functions for an effective delivery cascade for cancer drugs, Adv. Mater. 26 (45) (2014) 7615–7621.
[30] X. Guan, Z. Guo, L. Lin, J. Chen, H. Tian, X. Chen, Ultrasensitive pH triggered charge/size dual-rebound gene delivery system, Nano Lett. 16 (11) (2016) 6823–6831.
[31] T. Whiteside, The tumor microenvironment and its role in promoting tumor growth, Oncogene 27 (45) (2008) 5904.
[32] D.M. Gilkes, G.L. Semenza, D. Wirtz, Hypoxia and the extracellular matrix: drivers of tumour metastasis, Nat. Rev. Canc. 14 (6) (2014) 430.
[33] R. Kalluri, The biology and function of fibroblasts in cancer, Nat. Rev. Canc. 16 (9) (2016) 582.
[34] C. Bonnans, J. Chou, Z. Werb, Remodelling the extracellular matrix in development and disease, Nat. Rev. Mol. Cell Biol. 15 (12) (2014) 786.
[35] Y. Matsumoto, J.W. Nichols, K. Toh, T. Nomoto, H. Cabral, Y. Miura, R.J. Christie, N. Yamada, T. Ogura, M.R. Kano, Vascular bursts enhance permeability of tumour blood vessels and improve nanoparticle delivery, Nat. Nanotechnol. 11 (6) (2016) 533.
[36] A. Gabizon, D. Papahadjopoulos, Liposome formulations with prolonged circulation time in blood and enhanced uptake by tumors, Proc. Natl. Acad. Sci. Unit. States Am. 85 (18) (1988) 6949–6953.
[37] K. Otsuka, S.-i. Karato, Deep penetration of molten iron into the mantle caused by a morphological instability, Nature 492 (7428) (2012) 243.
[38] Y. Liu, D. Zhang, Z.Y. Qiao, G.B. Qi, X.J. Liang, X.G. Chen, H. Wang, A peptide--network weaved nanoplatform with tumor microenvironment responsiveness and deep tissue penetration capability for cancer therapy, Adv. Mater. 27 (34) (2015) 5034–5042.
[39] Y. Lu, A.A. Aimetti, R. Langer, Z. Gu, Bioresponsive materials, Nat. Rev. Mater. 2 (1) (2017) 16075.
[40] R.K. Jain, Normalization of tumor vasculature: an emerging concept in anti-angiogenic therapy, Science 307 (5706) (2005) 58–62.
[41] S. Mura, J. Nicolas, P. Couvreur, Stimuli-responsive nanocarriers for drug delivery, Nat. Mater. 12 (11) (2013) 991.
[42] S. Wang, P. Huang, X. Chen, Hierarchical targeting strategy for enhanced tumor tissue accumulation/retention and cellular internalization, Adv. Mater. 28 (34) (2016) 7340–7364.
[43] P. Zhang, Y. Wang, J. Lian, Q. Shen, C. Wang, B. Ma, Y. Zhang, T. Xu, J. Li, Y. Shao, Engineering the surface of smart nanocarriers using a pH-/thermal-/GSH-responsive polymer zipper for precise tumor targeting therapy in vivo, Adv. Mater. 29 (36) (2017).
[44] E. Blanco, H. Shen, M. Ferrari, Principles of nanoparticle design for overcoming biological barriers to drug delivery, Nat. Biotechnol. 33 (9) (2015) 941.
[45] V.P. Chauhan, T. Stylianopoulos, J.D. Martin, Z. Popović, O. Chen, W.S. Kamoun, M.G. Bawendi, D. Fukumura, R.K. Jain, Normalization of tumour blood vessels improves the delivery of nanomedicines in a size-dependent manner, Nat. Nanotechnol. 7 (6) (2012) 383–388.
[46] H. Maeda, J. Wu, T. Sawa, Y. Matsumura, K. Hori, Tumor vascular permeability and the EPR effect in macromolecular therapeutics: a review, J. Contr. Release 65 (1–2) (2000) 271–284.
[47] Z. Cheng, A. Al Zaki, J.Z. Hui, V.R. Muzykantov, A. Tsourkas, Multifunctional nanoparticles: cost versus benefit of adding targeting and imaging capabilities, Science 338 (6109) (2012) 903–910.
[48] S. Wilhelm, A.J. Tavares, Q. Dai, S. Ohta, J. Audet, H.F. Dvorak, W.C. Chan, Analysis of nanoparticle delivery to tumours, Nat. Rev. Mater. 1 (5) (2016) 16014.
[49] V.P. Torchilin, Multifunctional, stimuli-sensitive nanoparticulate systems for drug delivery, Nat. Rev. Drug Discov. 13 (11) (2014) 813.
[50] D. Ling, M.J. Hackett, T. Hyeon, Cancer imaging: lighting up tumours, Nat. Mater. 13 (2) (2014) 122.
[51] A. Martin-Herranz, A. Ahmad, H.M. Evans, K. Ewert, U. Schulze, C.R. Safinya, Surface functionalized cationic lipid-DNA complexes for gene delivery: PEGylated lamellar complexes exhibit distinct DNA-DNA interaction regimes, Biophys. J. 86 (2) (2004) 1160–1168.
[52] A. Aravind, P. Jeyamohan, R. Nair, S. Veeranarayanan, Y. Nagaoka, Y. Yoshida, T. Maekawa, D.S. Kumar, AS1411 aptamer tagged PLGA-lecithin-PEG nanoparticles for tumor cell targeting and drug delivery, Biotechnol. Bioeng. 109 (11) (2012) 2920–2931.
[53] J.F. Lovell, C.S. Jin, E. Huynh, H. Jin, C. Kim, J.L. Rubinstein, W.C. Chan, W. Cao, L.V. Wang, G. Zheng, Porphysome nanovesicles generated by porphyrin bilayers for use as multimodal biophotonic contrast agents, Nat. Mater. 10 (4) (2011) 324.
[54] A.D. Keefe, S. Pai, A. Ellington, Aptamers as therapeutics, Nat. Rev. Drug Discov. 9 (7) (2010) 537.
[55] E. Even-Sapir, U. Metser, E. Mishani, G. Lievshitz, H. Lerman, I. Leibovitch, The detection of bone metastases in patients with high-risk prostate cancer: 99mTc-MDP Planar bone scintigraphy, single-and multi-field-of-view SPECT, 18F-fluoride PET, and 18F-fluoride PET/CT, J. Nucl. Med. 47 (2) (2006) 287–297.